Clim. Past Discuss., 10, 4191–4227, 2014
www.clim-past-discuss.net/10/4191/2014/
doi:10.5194/cpd-10-4191-2014

Climate of the Past Discussions
Open Access

Carbon isotope ($\delta^{13}C$) excursions suggest times of major methane release during the last 14 ka in Fram Strait, the deep-water gateway to the Arctic

C. Consolaro[1,2], T. L. Rasmussen[1], G. Panieri[1], J. Mienert[1], S. Bünz[1], and K. Sztybor[1]

[1]CAGE – Centre for Arctic Gas Hydrate, Environment and Climate, Department of Geology, UiT the Arctic University of Norway, Dramsveien 201, 9037 Tromsø, Norway
[2]School of Geography, Earth & Environmental Sciences, Plymouth University, Drake Circus, Plymouth PL4 8AA, UK

Received: 16 September 2014 – Accepted: 29 September 2014 – Published: 24 October 2014

Correspondence to: C. Consolaro (chiara.consolaro@uit.no, chiara.consolaro@plymouth.ac.uk, chiara.consolaro@icloud.com)

Published by Copernicus Publications on behalf of the European Geosciences Union.

Abstract

We present results from a sediment core collected from a pockmark field on the Vestnesa Ridge (~ 80° N) in the eastern Fram Strait. This is the only deep-water gateway to the Arctic, and one of the northernmost marine gas hydrate provinces in the world. Eight ^{14}C AMS dating reveals a detailed chronology for the last 14 ka BP. The δ^{13}C record measured on the benthic foraminiferal species *Cassidulina neoteretis* shows two distinct intervals with negative values, as low as −4.37 ‰ in the Bølling–Allerød interstadials and as low as −3.41 ‰ in the early Holocene. After a cleaning procedure designed to remove all authigenic carbonate coatings on benthic foraminiferal tests, the ^{13}C values are still negative (as low as −2.75 ‰). We have interpreted these negative carbon isotope excursions (CIEs) to record past methane release events, resulting from the incorporation of ^{13}C-depleted carbon from methane emissions into the benthic foraminiferal shells. The CIEs during the Bølling–Allerød interstadials and the early Holocene relate to periods of ocean warming, sea level rise and increased concentrations of methane (CH_4) in the atmosphere. CIEs with similar timing have been reported from other areas in the North Atlantic suggesting a regional event. The trigger mechanisms for such regional events remain to be determined. We speculate that sea-level rise and seabed loading due to high sediment supply in combination with increased seismic activity as a result of rapid deglaciation may have triggered the escape of significant amounts of methane to the seafloor and the water column above.

1 Introduction

Methane hydrate is an ice-like compound that exists in sediments at high pressures and low temperatures with sufficient supply of water and gas (Sloan, 1998). Methane hydrate provinces are widespread in the Arctic region, but their stability and longevity through time, and the significance of their contribution to the global carbon budget are

CPD
10, 4191–4227, 2014

still poorly understood (e.g., Biastoch et al., 2011). The Arctic region is highly sensitive to climate change and the effects of the on-going global warming are probably more extreme in the Arctic than elsewhere (e.g., Screen and Simmonds, 2010; Spielhagen et al., 2011). Recent discoveries suggest that the stability of gas hydrates in the Arctic Ocean in water depths up to about 400 m is already affected by on-going ocean warming (e.g., Shakova et al., 2010; Ferré et al., 2012; Berndt et al., 2014). Methane emissions offshore west Svalbard from pockmarks in water depths greater than 800 m have been recently recorded in the eastern part of the Vestnesa Ridge (Figs. 1 and 2), where several additional gas plumes have been detected in 2010 (Bünz et al., 2012) and in 2012 (Smith et al., 2014), compared to the 2008 survey (Hustoft et al., 2009a), possibly indicating an increase in methane release activity. Therefore, it is critical to investigate the frequency of methane (CH_4) emissions through time, in relation to past climate change with a special focus on periods of climate warming.

It has been demonstrated that benthic foraminifera that lives close to active methane seep sites can register the low $\delta^{13}C$ methane-derived values in their tests (Wefer et al., 1994; Rathburn et al., 2003; Hill et al., 2004; Martin et al., 2004; Panieri et al., 2009, 2012, 2014a). Several sediment cores from the Vestnesa Ridge pockmark field in approximately 1200 m water depth offshore NW Svalbard are being investigated in order to reconstruct past methane emissions from the seafloor. This study is part of an ongoing research project at the Centre of Excellence for Arctic Gas Hydrate, Environment and Climate (CAGE) at the Arctic University of Norway (Panieri et al., 2014b; Sztybor et al., 2014). Here we present a detailed data analysis from a sediment core that was taken in a pockmark from the western part of the Vestnesa Ridge (Fig. 2). The core was investigated for stable isotopes (in particular $\delta^{13}C$), together with the distribution of planktic foraminifera and sedimentological parameters, in order to reconstruct the past methane activity in the area. Our results of the ^{14}C AMS (accelerator mass spectrometry) dating suggest an undisturbed sedimentary record for the last 14 ka BP. Negative carbon isotope excursions (CIEs) during the Bølling–

CPD
10, 4191–4227, 2014

Allerød interstadials and during the early Holocene provide important records of past methane release events.

2 Study area

The Vestnesa Ridge is an elongated sediment drift at ~ 80° N at the northwestern Svalbard margin in the eastern Fram Strait. The Fram Strait is dominated by two main surface currents: the warm West Spitsbergen Current (WSC) and the cold East Greenland Current (EGC) (Aagaard et al., 1987) (Fig. 1). The WSC is the northernmost branch of the North Atlantic Current (NAC) and brings warm, saline water along the western Svalbard margin and through the Fram Strait into the Arctic Ocean (e.g., Ferré et al., 2012). This current is the major source of heat and salt to high northern latitudes and is very important for the generation of deep water in the Nordic seas (Aagaard et al., 1985). The warm Atlantic water overlies the Greenland Sea Intermediate Water, which is generated from convection in the Nordic Seas (Aagaard et al., 1987). The EGC carries cold polar water and sea ice from the Arctic Ocean southwards along the East Greenland margin through the Denmark Strait and into the North Atlantic Ocean (Fig. 1).

The Vestnesa Ridge is located on hot, thin and young (< 20 Ma) oceanic crust (Fig. 2). (e.g. Hustoft et al., 2009a). It belongs to the eastern spreading segment of the Molloy Fracture Zone that is connected to the northernmost extension of the Mid-Atlantic Ridge system: the ultra-slow spreading Knipovich Ridge (Engen et al., 2008; Hustoft et al., 2009a) (Fig. 2a). The sediment crest of the Vestnesa Ridge is pierced with pockmarks (Fig. 2b) (e.g. Vogt et al., 1994; Hustoft et al., 2009a), which are seafloor craters formed in soft, fine-grained sediments, where localized seepage of gas and pore fluid occurs (Judd and Hovland, 2007). In seismic data, a bottom-simulating reflector (BSR) is present 160–180 m beneath the seabed and indicates the presence of gas hydrate in the subsurface (Hustoft et al., 2009a; Petersen et al., 2010; Bünz et al., 2012). Active gas venting has recently been observed in the eastern part

CPD
10, 4191–4227, 2014

of the ridge, where thermogenic free gas migrates to the crest of the BSR anticline and further upward to the Vestnesa Ridge pockmark field (Hustoft et al., 2009a; Bünz et al., 2012; Smith et al., 2014). Seismic data beneath the pockmark field shows vertical gas migration pathways, so-called chimneys that form conduits allowing the gas to bypass the hydrate stability zone (HSZ) and escape at the seafloor (Bünz et al., 2012). Acoustic observations of gas seeping from the pockmark fields in 1300 m water depth, in the deeper, western part of the ridge are lacking, inducing Bünz et al. (2012) to believe that these pockmarks are most probably inactive (Fig. 2b). The studied sediment core comes from such an inactive pockmark (Fig. 2b)

3 Material and methods

Gravity core JM10-330GC (79.13° N, 5.6° E; 420 cm long) was taken from about 1300 m water depth (mwd) in a pockmark located on the inactive western part of the Vestnesa Ridge (Figs. 1 and 2). Before opening of the core, magnetic susceptibility was measured with a Bartington MS2 loop sensor (Fig. 3). Afterwards the core was split longitudinally, one half was X-rayed and color imaged with a Jai L-107CC 3 CCD RGB Line Scan Camera installed on an Avaatech XRF core scanner (Fig. 3). The other half was sampled at 5 cm intervals in 1 cm thick slices, weighed and subsequently freeze-dried. Dry samples were weighed and wet sieved over mesh sizes of 63, 100 µm, and 1 mm. The residues were dried at 40 °C. Benthic and planktic foraminifera were picked from the > 100 µm size fraction, counted (at least 300 specimens) and identified to species level for assemblage analysis (in this paper we only present data on the two most dominant planktic species *Neogloboquadrina pachyderma* sinistral (s) and *Turborotalita quinqueloba*), AMS radiocarbon dating and isotope analysis. Ice Rafted Detritus (IRD) was counted in the > 1 mm size fraction (Fig. 3).

Eight ^{14}C AMS dates were performed on monospecific samples of *N. pachyderma* (s) (Table 1) at the Chrono Centre of Queen's University, Belfast, UK. The radiocarbon dates were calibrated to calendar years using the Calib 7.0 program (Stuiver et al.,

CPD
10, 4191–4227, 2014

2014) and the marine calibration curve Marine13 (Reimer et al., 2013) that operates with a standard reservoir correction of −400 years (Mangerud and Gulliksen, 1975). A regional correction of $\Delta R = 7 \pm 11$ years was applied, following the recommendations for planktic foraminifera dates by Bondevik and Gulliksen in Mangerud et al. (2006). The ages were calculated as the mid-point value from the calibrated age range ($\pm 2\sigma$). Calibrated dates are presented in years before present (BP) AD 1950 with SD 2σ. The age model was constructed assuming linear sedimentation between the calibrated dates (Fig. 3). The reservoir effect is probably not constant through time, and especially during the Younger Dryas it was probably larger (e.g., Bard et al., 1994; Bondevik et al., 2006; Austin et al., 2011). However, comparison between the stratigraphy of core JM10-330GC and the reference stratigraphy of the western Svalbard slope (Jessen et al., 2010), together with the distribution of planktic foraminifera and the oxygen isotope stratigraphy (Fig. 4), indicate that a standard reservoir correction age is appropriate.

Stable isotopes (oxygen and carbon; Supplementary Table S1) were measured on the planktic foraminifera species *N. pachyderma* (s) and on the benthic species *Cassidulina neoteretis*. Stable isotopes were performed at the Leibniz-Laboratory for Radiometric Dating and Isotope Research in Kiel, Germany, using a Finnigan MAT-253 mass spectrometer with Kiel IV system (analytical precision of ±0.05 ‰ for $\delta^{13}C$ and ±0.1 ‰ for $\delta^{18}O$). The $\delta^{18}O$ isotopic values were corrected for ice volume effect ($\delta^{18}O_{IVC}$; Table S1), using the Fairbanks (1989) sea-level curve as dated by Bard (1990) with a correction of 0.11 ‰ $\delta^{18}O$ per ten meters sea level change (subtracted from the measured $\delta^{18}O$ values).

Additional stable isotope analyses on cleaned benthic foraminifera samples from the lower part of the core (418–370 cm) were performed on a Thermo Finnigan MAT252 mass spectrometer coupled with a CarboKiel-II carbonate preparation device (analytical precision ±0.03 ‰ for $\delta^{13}C$ and ±0.08 ‰ for $\delta^{18}O$) at the Serveis Cientifico-Tècnics of the University of Barcelona (Table S1). The benthic foraminiferal samples have been cleaned following the protocol of Pena et al. (2005), which is adapted from

CPD
10, 4191–4227, 2014

Boyle and Rosenthal (1996). Prior to cleaning, the foraminifera were gently crushed between clean glass plates to break open individual chambers. The cleaning steps comprise: (1) removal of clays, Mn-Fe oxides and other mineral phases by a reductive cleaning step, (2) oxidative cleaning to eliminate organic matter, (3) weak acid leaching to remove remaining impurities from the shell surfaces. This protocol has proven to be efficient in removing the diagenetic carbonates attached to the foraminiferal shell (Pena et al., 2008; Panieri et al., 2012, 2014b).

The preservation state of the foraminifera tests were examined by Scanning Electron Microscope (SEM) in order to identify presence of authigenic carbonates and methane-derived deposits in selected representative specimens of *N. pachyderma* (s) and *C. neoteretis*. Qualitative estimates of the trace metal content were obtained from the test surface with Energy Dispersive X-ray Spectroscopy (EDS) (Table 2). SEM secondary electrons images and EDS spectra were acquired on a JEOL 6610 tungsten SEM equipped with an Oxford Instrument AzTEC EDS system in the Electron Microscopy Center, Plymouth University, UK.

4 Results

4.1 Chronology and lithology

Based on the calibrated ^{14}C dates, the distribution patterns of polar and subpolar planktic foraminifera species (Fig. 4a), and the benthic and planktic $\delta^{18}O$ records (Fig. 4b–d), we have correlated core JM10-330GC to the Greenland ice core event stratigraphy (Fig. 4), applying the new Greenland Ice Core Chronology 2005 (GICC05) of Rasmussen et al. (2006). The GICC05 time scale is b2k (before 2000 yr), therefore to compare it with the calendar ages (AD before 1950) used in this paper, we have subtracted 50 yr from the GICC05 time scale. In this new chronology the different periods are defined as followed: end of Bølling interstadial: 14.025 ka; onset of Younger Dryas (YD) stadial: 12.85 ka; YD-Holocene transition: 11.65 ka.

CPD
10, 4191–4227, 2014

Our age model shows that the core contains postglacial sediments covering the last 14 ka, spanning from the upper part of the Bølling–Allerød (B–A) interstadial periods to Recent (Figs. 3 and 4). The lithology (Fig. 3) is very similar to the reference core of the western Svalbard margin (Jessen et al., 2010), with the lower part (418–335 cm; 14.1–11.1 ka; B–A and YD interval) characterized by high concentration of ice-rafted debris (IRD) and common pyritized burrows indicative of bioturbation, with a greenish sandy layer at the beginning of the YD (360 cm; 12.7 ka). There is a fine-grained, structureless, silty mud interval with high abundance of diatoms in the middle part (335–225 cm; 11.1–8.8 ka, labeled diatom rich mud in Fig. 4). A homogeneous hemipelagic, grey clay with very little amount of IRD is present in the upper interval (225–0 cm; 8.8 ka to present).

The sedimentation rate is higher during the B–A period ($\sim 38\,\mathrm{cm\,ka^{-1}}$) and in the early Holocene ($42–50\,\mathrm{cm\,ka^{-1}}$), but lower during the Younger Dryas (YD: $\sim 18\,\mathrm{cm\,ka^{-1}}$) and after 7.5 ka ($19–26\,\mathrm{cm\,ka^{-1}}$) (Fig. 3; Table 1).

4.2 Carbon isotope excursions (CIEs)

During the Bølling–Allerød interstadials the δ^{13}C record of the infaunal benthic foraminifera *C. neoteretis* shows values considerably lower than the average core value of −1.10 ‰ (CIE I). The low values occur at about 13.9 ka (−2.87 ‰) and at 13.5 ka (−4.37 ‰), and another but less pronounced low value at 12.9 ka (−2.21 ‰; Fig. 4e). The planktic *N. pachyderma* (s) δ^{13}C values are generally lower than the average core value of 0.10 ‰, and show one prominent excursion (−2.61 ‰) at 13.5 ka (Fig. 4c).

Another interval with low benthic δ^{13}C values occurs in the early part of the Holocene (CIE II; Fig. 4e). This event lasted approximately 500 years (ca. 10.5–10 ka) and is characterized by benthic δ^{13}C values that are lower than −2 ‰, with the most prominent excursion at 10.3 ka (−3.41 ‰). CIE II is not recorded in the planktic record, where the δ^{13}C values are very close to the average core value and within the normal range of the marine environment (Fig. 4c).

CPD
10, 4191–4227, 2014

The $\delta^{13}C$ values in both benthic and planktic records between the two events (from about 12.8 to 10.5 ka) are very close or slightly lower than average values, whereas after 9 ka they are higher than the average values (Fig. 4c–e).

The $\delta^{18}O_{IVC}$ benthic and planktic records present little variability if compared to the average values of 4.35 and 3.12 ‰, respectively (Fig. 4b–d). Light isotope excursions are present in both the benthic (< 0.7 ‰ lighter than the average) and planktic record (about 1.2 ‰ lighter than the average) during the Younger Dryas and are probably related to a melt water event, which is also documented by a sandy layer. No light isotopic excursions are associated with CIE I, and in the early Holocene only two relatively light (< 0.7 ‰ lighter than the average) excursions exist in the $\delta^{18}O$ benthic record at the beginning and at the end of CIE II (Fig. 4).

5 Discussion

5.1 CIEs: secondary overgrowth vs. primary tests

The benthic foraminiferal (*C. neoteretis*) $\delta^{13}C$ record shows negative excursions in the Bølling–Allerød interstadials (CIE I) and in the early Holocene (CIE II). These values are 1–3.3 ‰ lower than the average value of −1.10 ‰ in the sediment core, which is comparable to values of *C. neoteretis* recovered from the same region, but in sites unaffected by methane seepage (ca. −1 to 0 ‰ in the northern Barents Sea: Wollenburg et al., 2001; −1.15 ‰ in the control site away from Håkon Mosby mud volcano in the Barents Sea; Mackensen et al., 2006).

The planktic foraminifera $\delta^{13}C$ record show similar negative trend during CIE I (Fig. 4c), with lower values compared to the normal $\delta^{13}C$ range of *N. pachyderma* (s) in the same region (between ca. −0.5 and 1 ‰: Volkmann and Mensch, 2001; Nørgaard–Pedersen et al., 2003; Sarnthein et al., 2003; Jessen et al., 2010).

The negative values in both species can be attributed to diagenetic alteration that may stem from AOM (Anaerobic Oxidation of Methane)-derived authigenic carbonates

CPD
10, 4191–4227, 2014

on the foraminiferal tests after their deposition on the seafloor (Torres et al., 2003, 2010; Millo et al., 2005b; Panieri et al., 2009).

Therefore, in order to distinguish the isotopic records of the secondary overgrowth from the primary tests, we have repeated the isotopic analyses on cleaned *C. neoteretis* specimens from the CIE I (see Sect. 3). The repetition of the isotopic analyses for *N. pachyderma* (s) and for *C. neoteretis* from the CIE II interval was impossible because of lack of material. Thus a detailed SEM investigation was done on both species (see below).

The δ^{13}C values obtained after the cleaning are higher (by up to 1.6‰) compared to the tests cleaned with the standard protocol, but are still low (Table S1; Fig. 5). The values (as low as −2.75‰) are significantly lower than the core average (−1.10‰) and also lower compared to the δ^{13}C records of *C. neoteretis* of the last deglaciation from the same region (ca. −0.5 to 0.3‰ in the Kara Sea (Lubinski et al., 2001); ca. −1 to 0‰ in the N Barents Sea (Wollenburg et al., 2001); ca. 0 to 1.5‰ in the SW Barents Sea, Aagaard-Sørensen et al., 2010). Dead specimens (empty tests) of *C. neoteretis* from surface samples at the active Håkon Mosby mud volcano in the Barents Sea show very similar δ^{13}C negative values (from −1.65 to −2.82‰) (Mackensen et al., 2006). We interpret the low values of the primary tests as indicative of the incorporation of ^{13}C-depleted carbon in presence of methane seepage at the seafloor during primary bio-mineralization (e.g. Rathburn et al., 2003; Hill et al., 2004; Panieri et al., 2014a). The ^{13}C-depleted values of diagenetic overgrowth on shells of *C. neoteretis* are cumulatively added to the already negative values of the foraminifera. This is also evident considering that the δ^{13}C values of *N. pachyderma* (s) are less negative (about 1.7‰) compared to the δ^{13}C values of *C. neoteretis*.

N. pachyderma (s) in the early Holocene (CIE II) exhibit values in the normal marine range (> −0.5‰). Differently from CIE I, no diagenetic overgrowth has affected the dead planktic and benthic foraminiferal assemblages during CIE II. This confirms that *C. neoteretis* secrete the calcitic tests using light carbon from methane seepage at the seafloor.

CPD
10, 4191–4227, 2014

5.2 SEM investigations

Negative $\delta^{13}C$ methane signals are not expected to be registered in planktic foraminifera because they float in the water column, transported by the ocean currents, and most of the methane should be consumed during anaerobic oxidation of methane (AOM) in the sediment (Reeburgh, 1980; Iversen and Jørgensen, 1985) and by methanotrophic bacteria in the water column (Reeburgh, 2007). The negative values of *N. pachyderma* (s) during CIE I may therefore be related to the precipitation of AOM-derived authigenic deposits on the foraminiferal tests.

The SEM pictures of *N. pachyderma* (s) from the most negative peak of CIE I (−2.61 ‰, 390 cm bsf at 13.5 ka) show, indeed, evidence of an altered test (Fig. 6a and b) with a thin, uneven coating (< 1µm) on the test surface (Fig. 6c). The Energy Dispersive X-ray Spectroscopy (EDS) estimates on the composition of the external test suggest that it consists of $CaCO_3$ constituting > 96.75 weight percent (wt%) with minor amounts of Mg, Na, Al and Si (< 1.5 wt%, EDS 1 in Table 2). The deposited layer consists mainly of SiO_2 (40–41 wt%), enriched in Al, Fe, K and Mg with only 6.5 to 8.5 wt% of $CaCO_3$ (EDS 2 and 3 in Table 2). Conversely, the internal part of the wall looks unaltered with pristine crystal palisades consisting of $CaCO_3$ (> 99 wt%) with only minor amounts of Na (EDS 4 and 5 in Table 2). The composition of the coating is very similar to the composition of the overgrowth portion on altered tests of *N. pachyderma* (s) from depleted ^{13}C intervals in the southwestern Greenland Sea (Millo et al., 2005b). We have interpreted the coating on the of *N. pachyderma* (s) test (Fig. 6c) as AOM-derived authigenic deposits.

The *N. pachyderma* (s) tests from CIE II (−0.02 ‰, 295 cm bsf at 10.3 ka) and from the late Holocene (0.68 ‰, 80 cm bsf at 4.1 ka) are well preserved with pristine shell structure (Fig. 6d, e, g and h) and walls characterized by crystal palisades (Fig. 6f–i). The composition of the test is mainly $CaCO_3$ (97–99.7 wt%) with only minor traces of Na, Mg, Si and Al (EDS 6–9 and 10–12 in Table 2).

CPD
10, 4191–4227, 2014

No evident coating has been detected on the benthic foraminiferal tests in both depleted intervals (390 and 295 cm bsf; Fig. 7j–o), where the alteration mainly consists of dissolution and corrosion features probably due to an increase in CO_2 during the AOM in marine sediments. EDS estimates indicate that the tests are composed mainly of $CaCO_3$ with Na, Si, Al and Mg between 0.5 and 4 wt% in the altered intervals (EDS 13–19 in Table 2), and only 0.5–0.7 wt% of Na in the unaltered interval (EDS 20–22 in Table 2). Clear indication of authigenic overgrowth is present only in the planktic foraminiferal tests from the most depleted interval (390 cm, 13.5 ka). This is probably because of the higher porosity and surface area of the *N. pachyderma* (s) tests, which are more likely to accommodate contamination and crystalline overgrowth than the smooth and imperforate test of *C. neoteretis*, as already observed by Cook et al. (2011).

5.3 CIEs: evidence for methane release

In the interval with negative $\delta^{13}C$ excursions in both benthic and planktic foraminifera (CIE I), the methane activity must have been strong enough and long enough as to induce AOM in pore-waters at shallow subsurface depths, and causing significant precipitation of AOM-derived deposits on the foraminiferal tests. In the intervals where only the benthic $\delta^{13}C$ record exhibits negative excursions (CIE II), the methane flux was probably less intense, diffusive and more localized, with very little or no formation of AOM-driven authigenic carbonates. Similar findings have been reported from the Nyegga pockmark field on the mid-Norwegian margin (Hill et al., 2012).

These data, together with the $\delta^{18}O$ values which are within the normal range for marine carbonates during CIE I and II, and considering that low $\delta^{13}C$ values occur in discrete stratigraphic intervals separated by values in the normal marine range, strongly suggest that the AOM-derived coating was formed at the same time, i.e. with the primary mineralization of the foraminifera tests or immediately after their deposition (in the case of planktic foraminifera). Similar events with much lighter ^{13}C values (as low as −17.4 ‰) have been reported from coeval deposits in two active pockmarks on the eastern part of the Vestnesa Ridge (Panieri et al., 2014b; Sztybor et al., 2014).

CPD
10, 4191–4227, 2014

5.4 North Atlantic deglacial CIEs

Similar ^{13}C depletions in the foraminiferal record have been reported in several Quaternary isotope records and have been interpreted as evidence for methane release (Kennett et al., 2000; Smith et al., 2001; Keigwin, 2002; Millo et al., 2005a; Cook et al., 2011; Hill et al., 2012). In particular, low $\delta^{13}C$ values during the Bølling–Allerød interstadials (15–13 ka) and during the early Holocene (10.5–9 ka) have been reported in stable isotope records from the East Greenland continental shelf (500 mwd; JM96 cores in Fig. 1) (Smith et al., 2001) and from the Nyegga pockmark field on the mid-Norwegian margin (800–1000 mwd; NPF in Fig. 1) (Hill et al., 2012). The similarity in timing of these events over long distances and wide water depth ranges (Fig. 1) is remarkable and suggests that the CIEs are regional at the scale of the North Atlantic Ocean to the Fram Strait.

Both the B–A interstadials and the early Holocene are periods of climate warming during the deglaciation (NGRIP Members, 2004; Fig. 4f) and are characterized by increased CH_4 concentration in the atmosphere (Brook et al., 2000; GISP2, Fig. 4g). They also occur during periods of rapid sea-level rise (melt water pulse-mwp-1A: 14.3–12.8 ka; mwp-1B: 11.5–8.8 ka) (Peltier and Fairbanks, 2006; Stanford et al., 2011; Fig. 4h). These findings suggest an apparent correlation between methane events in the North Atlantic and the Fram Strait, and climatic events at global or regional scale.

5.5 Possible triggering mechanisms and connection with climate change?

It is still not possible to determine if present-day gas emissions at the eastern part of the Vestnesa Ridge are sourced from below the HSZ (Hydrate Stability Zone), directly from hydrate dissociation, or from a combination of deeper and shallower processes (Bünz et al., 2012; Smith et al., 2014). It is also unclear whether focused fluid flow pathways from the base of the HSZ have been established recently at the end of the last glaciation or whether they have existed for much longer and have been reactivated multiple times. Even though this study has only documented two former emission

CPD
10, 4191–4227, 2014

events at the western end of the Vestnesa Ridge, it favors a model of reactivation of chimney structures. The timing of the gas emissions and reactivation seem to occur during periods of climate change similar to what has been observed on the mid-Norwegian margin, where the generation and initiation of focused fluid flow is likely related to an overpressure due to a combined effect of loading of glacigenic sediments and shelf ice glaciation (Hustoft et al., 2009b; Plaza-Faverola et al., 2011). However, the initial generation of such chimney structures and their reactivation might each be related to different geological processes. Chimneys are usually conceived as a network of connected small-scale fractures originating from natural hydraulic fracturing (Arntsen et al., 2007). They represent pre-existing zones of weakness and open pathways that might facilitate fluid flow much more easily than during the initial generation of the fracture network. In deep-water areas these fractures might be filled with gas hydrate (Kim et al., 2011).

The climate forcing of gas emission in the western part of the Vestnesa Ridge documented herein could be the result of the individual or combined effect of sea-level rise, increased seismicity, elevated sedimentation rates and/or gas hydrate dissociation. From the above mentioned processes it seems unlikely that gas hydrate dissociation and loading of glacigenic sediment have played a major role given that our study area is in deep-water, far away from the shelf edge and that the timing of the deposition of large amount of glacigenic sediments (Ottesen et al., 2005; Mattingsdal et al., 2014) does not coincide with the venting periods documented herein.

Both carbon isotopes excursions (CIIEs) occur at times when deep convection and generation of cold bottom water is strong (McManus et al., 2004; Ezat et al., 2014). The high $\delta^{18}O_{ICV}$ values of the benthic record during CIE I confirm that the area was bathed in cold water during the B–A interval (Fig. 4d). During CIE II, the marked shift in the planktic assemblage (previously dominated by the polar species *N. pachyderma* (s) and now by the subpolar species *T. quinqueloba*, Fig. 4a) indicates a surface water warming. The presence of two relatively light excursions of benthic $\delta^{18}O_{ICV}$ (< 0.7 ‰; Fig. 4d) indicate a small warming of the bottom water, but certainly too small to start

CPD
10, 4191–4227, 2014

gas hydrate dissociation (see Rasmussen et al., 2007, 2014; Ezat et al., 2014; Groot et al., 2014). Hydrate dissociation at such depth would require a substantial warming before any gas can escape from deeper buried sediments (> 1000 mwd) (Reagan and Moridis, 2007), although hydrates buried at shallower depth within chimneys could be affected to some extent and release gas at the seabed.

The present sedimentation rate on the Vestnesa Ridge is about 19 cm ka^{-1} whereas, during the deglaciation, it was considerably higher (40–50 cm ka^{-1}; Fig. 3 and Table 1). Around 14.6 to 14.3 ka sedimentation rates on the western Svalbard margin increased over large areas to > 5 m ka^{-1} (Jessen et al., 2010 and references therein). It is however, not known if such a relatively small loading alone could have significantly increased fluid overpressure in the subsurface resulting in methane release at the seabed.

Sea-level on the other hand has risen considerably after the last glaciation and the two documented emission periods correlate well with two major melt water pulses (mwp-1A and -1B; Fig. 4h; Peltier and Fairbanks, 2006; Stanford et al., 2011). Global sea level rise has been implicated in triggering of landslides by causing an increase in excess pore pressure in the subseafloor (Owen et al., 2007; McGuire and Maslin, 2012). However, the hydrostatic pressure increase would only affect excess pore pressures if impermeable sediments or a complex subsurface structure traps the pores. These trapping mechanisms might be provided by gas hydrates that clog the pore space along the BSR or fill the fractures of gas chimneys (Nimblett et al., 2003; Kim et al., 2011). Potentially a cumulative effect of sedimentation and sea-level rise has elevated excess pore pressure to initiate gas migration along the fracture network within a chimney.

Moreover, sea level rise, elevated sedimentation rates in the whole study area and the isostatic rebound following the retreat of the glaciers (Landvik et al., 1998; Forman et al., 2004; Bungum et al., 2005) may foster other processes, such as lithospheric stress changes resulting in increased seismicity. Modeling studies (Wallmann et al., 1988; Nakada et al., 1992) have demonstrated that sea-level changes are capable

CPD
10, 4191–4227, 2014

of triggering or modulating tectonic activity. More specifically, Lutrell and Sandwell (2010) have shown that lithospheric flexure due to ocean loading caused by post-glacial sea-level rise was sufficient to promote failure through the reduction of normal stress thereby reactivating faults.

Increased seismicity might have had a two-fold effect on the fluid flow system in the Vestnesa Ridge. It might have led to an increased supply of gas along deep-seated faults leading to an increase in pore pressures beneath the hydrate-bearing sediments. Furthermore, it might have led to an excitation and dilation of fractures within the chimney structures leading to the leakage of gas, similar to what has been observed on the Bear Island Fan (Franek et al., 2014).

We cannot conclusively distinguish what has triggered gas venting in two periods at the end of and shortly after the last glaciation, but suggest that a combined effect of sea-level rise, sedimentation and seismicity might have led to increased pore pressures in an already over-pressured system, thereby promoting and initiating gas venting from the seabed at the western part of the Vestnesa Ridge.

6 Conclusions

We have presented new data from a sediment core collected in the eastern part of the Fram Strait at Vestnesa Ridge, a site where deep-water flows into the Arctic Ocean. Here, inactive and active pockmark fields exist whereas the sediment core was retrieved from an inactive pockmark in the western, deeper part of the Vestnesa Ridge. The results show a surprisingly undisturbed sedimentary record that allows establishing a detailed methane release event chronology for the last 14 ka. The benthic $\delta^{13}C$ record shows negative carbon isotope excursions (CIE) as low as −4.37 ‰ during the Bølling–Allerød interstadials (CIE I) and as low as −3.41 ‰ in the early Holocene (CIE II). The persistence of negative values (as low as −2.75 ‰) after a thorough cleaning procedure, which was designed to remove all authigenic carbonate coatings on benthic foraminiferal tests from CIE I samples, demonstrate that

CPD
10, 4191–4227, 2014

^{13}C-depleted values of diagenetic overgrowth on *C. neoteretis* are cumulatively added to the already negative values of the primary test.

The planktic foraminifera δ^{13}C record shows similar negative trend during the CIE I (with values as low as −2.61 ‰), but during CIE II the values are within the normal marine range (−0.5 to 1 ‰). SEM investigations confirm the presence of a thin AOM-derived coating on the *N. pachyderma* tests exclusively during CIE I.

We have interpreted both CIEs to record past methane release events based on the incorporation of ^{13}C-depleted carbon from methane emissions at sea floor during the biomineralization of the carbonate foraminiferal tests, with subsequent secondary mineralization only during CIE I.

The derived methane signals in our records are weaker if compared to active sites in the eastern part of the Vestnesa Ridge, where main methane events show values as low as −17.4 ‰ (Panieri et al., 2014b; Sztybor et al., 2014).

Methane release events with similar timing have been reported in several locations in the North Atlantic and together with our new observation point to a more regional event, showing an apparent correlation to northern climatic events.

We suggest that a combined effect of sea-level rise, high sediment loading and increased seismicity during the deglaciation could have led to increased pore pressures, and therefore promoting and initiating gas venting from the seafloor in the Vestnesa Ridge, eastern Fram Strait. The methane contribution from the ocean floor to the water column and to the atmosphere remains to be quantified.

The Supplement related to this article is available online at doi:10.5194/cpd-10-4191-2014-supplement.

Acknowledgements. This research is part of the Centre of Excellence: Arctic Gas hydrate, Environment and Climate (CAGE) funded by the Norwegian Research Council (grant no. 223259). Additional funding came from the European project HERMIONE of the 7th framework program environment including climate change (grant no. 226354). We are grateful to the

CPD
10, 4191–4227, 2014

captain, crew and scientific party onboard R/V *Helmer Hanssen* for help in collecting the core. We thank the staff at the Electron Microscopy Centre at Plymouth University (UK) for assistance during SEM and EDS analysis. We acknowledge the assistance of J. P. Holm for Fig. 1.

References

Aagaard, K., Swift, J. H., and Carmack, E. C.: Thermohaline circulation in the Arctic Mediterranean Seas, J. Geophys. Res., 90, 4833–4846, 1985.

Aagaard, K., Foldvik, A., and Hillman, S. R.: The West Spitsbergen Current: disposition and water mass transformation, J. Geophys. Res., 92, 3778–3784, 1987.

Arntsen, B., Wensaas, L., Loseth, H., and Hermanrud, C.: Seismic modeling of gas chimneys, Geophysics, 72, 251–259, 2007

Austin, W. E. N., Telford, R. J., Ninnemann, U. S., Brown, L., Wilson, L. J., Small, D. P., and Bryant, C. L.: North Atlantic reservoir ages linked to high Younger Dryas atmospheric radiocarbon concentrations, Global Planet. Change, 79, 226–233, 2011.

Bard, E., Arnold, M., Mangerud, J., Paterne, M., Labeyrie, L., Duprat, J., Mélières, M.-A., Sønstegaard, E., and Duplessy, J.-C.: The North Atlantic atmosphere-sea surface ^{14}C gradient during the Younger Dryas climatic event, Earth Planet. Sc. Lett., 126, 275–287, 1994.

Berndt, C., Feseker, T., Treude, T., Krastel, S., Liebetrau, V., Niemann, H., Bertics, V. J., Dumke, I., Dünnbier, K., Ferré, B., Graves, C., Gross, F., Hissmann, K., Hühnerbach, V., Krause, S., Lieser, K., Schauer, J., and Steinle, L.: Temporal constraints on hydrate-controlled methane seepage off Svalbard, Science, 343, 284–287, 2014.

Biastoch, A., Treude, T., Rüpke, L. H., Riebesell, U., Roth, C., Burwicz, E. B., Park, W., Latif, M., Böning, C. W., Madec, G., and Wallmann, K.: Rising Arctic Ocean temperatures cause gas hydrate destabilization and ocean acidification, Geophys. Res. Lett., 38, L08602, doi:10.1029/2011GL047222, 2011.

Bondevik, S., Mangerud, J., Birks, H. H., Gulliksen, S., and Reimer, P.: Changes in North Atlantic radiocarbon reservoir ages during the Allerød and Younger Dryas, Science, 312, 1514–1517, 2006.

Boyle, E. A. and Rosenthal, Y.: Chemical hydrography of the south Atlantic during the Last Glacial Maximum: Cd vs. $\delta^{13}C$, in: The South Atlantic: Present and Past Circulation, edited

CPD
10, 4191–4227, 2014

by: Wefer, G., Berger, W. H., Siedler, G., and Webb, D., Springer-Verlag, Berlin, 423–443, 1996.
Brook, E. J., Harder, S., Severinghaus, J., Steig, E. J., and Sucher, C. M.: On the origin and timing of rapid changes in atmospheric methane during the last glacial period, Global Biogeochem. Cy., 14, 559–572, 2000.
Bungum, H., Lindholm, C., and Faleide, J. I.: Postglacial seismicity offshore mid-Norway with emphasis on spatio-temporal-magnitudal variations, Mar. Petrol. Geol., 22, 137–148, 2005.
Bünz, S., Polyanov, S., Vadakkepuliyambatta, S., Consolaro, C., and Mienert, J.: Active gas venting trough hydrate-bearing sediments on the Vestnesa Ridge, offshore W-Svalbard, Mar. Geol., 332–334, 189–197, 2012.
Cook, M. S., Keigwin, L. D., Birgel, D., and Hinrichs, K.-U.: Repeated pulses of vertical methane flux recorded in glacial sediments from the southeast Bering Sea, Paleoceanography, 26, PA2210, doi:10.1029/2010PA001993, 2011.
Ezat, M., Rasmussen, T. L., and Groeneveld, J.: Persistent intermediate water warming during cold stadials in the southeastern Nordic seas during the past 65 k.y., Geology, 42, 663–666, doi:10.1130/G35579.1, 2014.
Engen, Ø., Faleide, J. I., and Dyreng, T. K.: Opening of the Fram Strait gateway: a review of plate tectonic constraints, Tectonophysics, 450, 51–69, 2008.
Fairbanks, R. G.: A 17,000-year glacio-eustatic sea level record: influence of glacial melting rates on the Younger Dryas event and deep-ocean circulation, Nature, 342, 637–742, 1989.
Ferré, B., Mienert, J., and Feseker, T.: Ocean temperature variability for the past 60 years in the Norwegian-Svalbard margin influences gas hydrate stability on human time scale, J. Geophys. Res., 117, C10017, doi:10.1029/2012JC008300, 2012.
Forman, S. L., Lubinski, D. J., Ingólfsson, Ó., Zeeberg, J. J., Snyder, J. A., Siegert, M. J., and Matishov, G. G.: A review of postglacial emergence on Svalbard, Franz Josef Land and Novaya Zemlya, northern Eurasia, Quaternary Sci. Rev., 23, 1391–1434, 2004.
Franek, P., Mienert, J., Bünz, S., and Géli, L.: Character of seismic motion at a location of a gas hydrate-bearing mud volcano on the SW Barents Sea margin, J. Geophys. Res.-Sol. Ea., 119, 2014JB010990, 2014.
Groot, D. E., Aagaard-Sørensen, S., and Husum, K.: Reconstruction of Atlantic water variability during the Holocene in the western Barents Sea, Clim. Past, 10, 51–62, doi:10.5194/cp-10-51-2014, 2014.

CPD
10, 4191–4227, 2014

Hill, T. M., Kennett, J. P., and Valentine, D. L.: Isotopic evidence for the incorporation of methane-derived carbon into foraminifera from modern methane seeps, Hydrate Ridge, Northeast Pacific, Geochim. Cosmochim. Ac., 68, 4619–4627, 2004.

Hill, T. M., Paull, C. K., and Crister, R. B.: Glacial and deglacial seafloor methane emissions from pockmarks on the northern flank of the Storegga Slide complex, Geo.-Mar. Lett., 32, 73–84, 2012.

Hustoft, S., Bunz, S., Mienert, J., and Chand, S.: Gas hydrate reservoir and active methane-venting province in sediments on < 20 Ma young oceanic crust in the Fram Strait, offshore NW-Svalbard, Earth Planet. Sc. Lett., 284, 12–24, 2009a.

Hustoft, S., Dugan, B., and Mienert, J.: Effects of rapid sedimentation on developing the Nyegga pockmark field: constraints from hydrological modeling and 3-D seismic data, offshore mid-Norway, Geochem. Geophy. Geosy., 10, Q06012, doi:10.1029/2009GC002409, 2009b.

Iversen, N., Jørgersen, B. B., Anaerobic methane oxidation rates at the sulfate-methane transition in marine sediments from Kattegat and Skagerrak (Denmark), Limnol. Oceanogr., 30, 944–955, 1985.

Jessen, S. P., Rasmussen, T. L., Nielsen, T., and Solheim, A.: A new Late Weichselian and Holocene marine chronology for the western Svalbard slope 30,000–0 cal years, Quaternary Sci. Rev., 29, 1301–1312, 2010.

Judd, A. G. and Hovland, M.: Seabed Fluid Flow: The Impact on Geology, Biology, and the Marine Environment, Cambridge University Press, Cambridge, UK, 475 pp., 2007.

Keigwin, L. D.: Late Pleistocene-Holocene paleoceanography and ventilation of the Gulf of California, J. Oceanogr., 58, 421–432, 2002.

Kennett, J. P., Cannariato, K. G., Hendy, I. L., and Behl, R. J.: Carbon isotopic evidence for methane hydrate instability during Quaternary interstadials, Science, 288, 128–133, 2000.

Kim, G. Y., Yi, B. Y., Yoo, D. G., Ryu, B. J., and Riedel, M.: Evidence of gas hydrate from downhole logging data in the Ulleung Basin, East Sea, Mar. Petrol. Geol., 28, 1979–1985, 2011.

Landvik, J. Y., Bondevik, S., Elverhøi, A., Fjeldskaar, W., Mangerud, J., Salvigsen, O., Siegert, M. J., Svendsen, J.-I., and Vorren, T. O.: The last Glacial Maximum of Svalbard and the Barents Sea area: ice sheet extent and configuration, Quaternary Sci. Rev., 17, 43–75, 1998.

Luttrell, K., Sandwell, D.: Ocean loading effects on stress at near shore plate boundary fault systems, J. Geophys. Res., 115, B08411, doi:10.1029/2009JB006541, 2010.

CPD
10, 4191–4227, 2014

Mackensen, A., Wollenburg, J., and Licari, L.: Low δ^{13}C in tests of live epibenthic and endobenthic foraminifera at a site of active methane seepage, Paleocenography, 12, PA2022, doi:10.1029/2005PA001196, 2006.
Mangerud, J. and Gulliksen, S.: Apparent radiocarbon ages of recent marine shells from Norway, Spitsbergen, and Arctic Canada, Quaternary Res., 5, 263–273, 1975.
Mangerud, J., Bondevik, S., S. Gulliksen, S., Hufthammer, A. K., and Høisæter, T.: Marine ^{14}C reservoir ages for 19th century whales and molluscs from the North Atlantic, Quaternary Sci. Rev., 25, 3228–3245, 2006.
Martin, R. A., Nesbitt, E. A., Campbell, K. A.: The effect of anaerobic methane oxidation on benthic foraminiferal assemblages and stable isotopes on the Hikurangi Margin of eastern New Zealand, Mar. Geol., 272, 270–284, 2010.
Mattingsdal, R., Knies, J., Andreassen, K., Fabian, K., Husum, K., Grøsfjeld, De Schepper, S.: A new 6 Myr stratigraphic framework for the Atlantic-Arctic Gateway, Quaternary Sci. Rev., 92, 170–178, 2014.
McGuire, B. and Maslin, M.: Climate Forcing of Geological Hazards, John Wiley & Sons, Ltd, Chichester, UK, 328 pp., 2012
McManus, J. F., Francois, R., Gherardi, J.-M., Keigwin, L. D., and Brown-Ledger, S.: Collapse and rapid resumption of Atlantic meridional circulation linked to deglacial climate changes, Nature, 428, 834–837, 2004.
Millo, C., Sarnthein, M., Erlenkeuser, H., and Frederichs, T.: Methane-driven late Pleistocene δ^{13}C minima and overflow reversals in the southwestern Greenland Sea, Geology, 33, 873–876, 2005a.
Millo, C., Sarnthein, M., Erlenkeuser, H., Grootes, P. M., and Andersen, N.: Methane-induced early diagenesis of foraminiferal tests in the southwestern Greenland Sea, Mar. Micropaleontol., 58, 1–12, 2005b.
Nakada, M. and Yokose, H.: Ice age as a trigger of active Quaternary volcanism and tectonism, Tectonophysics, 212, 321–329, 1992.
Nimblett, J. and Ruppel, C.: Permeability evolution during the formation of gas hydrates in marine sediments, J. Geophys. Res., 108, 2420, doi:10.1029/2001JB001650, 2003.
North Greenland Ice Core Project Members: High-resolution record of Northern Hemisphere climate extending into the last interglacial period, Nature, 431, 147–151, 2004.
Nørgaard-Pedersen, N., Spielhagen, R. F., Erlenkeuser, H., Grootes, P. M., Heinemeier, J., and Knies, J.: Arctic Ocean during the Last Glacial Maximum: atlantic water and polar

CPD
10, 4191–4227, 2014

domains of surface water mass distribution and ice cover, Paleoceanography, 18, 1063, doi:10.1029/2002PA000781, 2003.
Ottesen, D., Dowdeswell, J. A., and Rise, L.: Submarine landforms and the reconstruction of fast-flowing ice streams within a large Quaternary ice sheet: the 2500-km-long Norwegian-Svalbard margin (57 degrees–80 degrees N), Geol. Soc. Am. Bull., 117, 1033–1050, 2005.
Owen, M., Day, S., and Maslin, M.: Late Pleistocene submarine mass movements: occurrence and causes, Quaternary Sci. Rev., 26, 958–978, 2007.
Panieri, G., Camerlenghi, A., Conti, S., Pini, G. A., and Cacho, I.: Methane seepages recorded in benthic foraminifera from Miocene seep carbonates, Northern Apennines (Italy), Palaeogeogr. Palaeocl., 284, 271–282, 2009.
Panieri, G., Camerlenghi, A., Cacho, I., Carvera, C. S., Canals, M., Lafuerza, S., and Herrera, G.: Tracing seafloor methane emissions with benthic foraminifera: results from the Ana submarine landslide (Eivissa Channel, Western Mediterranean Sea), Mar. Geol., 291–294, 97–112, doi:10.1016/j.margeo.2011.11.005, 2012.
Panieri, G., Aharun, P., Sen Gupta, B. K., Camerlenghi, A., Palmer Ferrer, F., and Cacho, I.: Late Holocene foraminifera of Blake Ridge diapir: assemblage variation and stable-isotope record in gas-hydrate bearing sediments, Mar. Geol., 353, 99–107, 2014a.
Panieri, G., James, R. H., Camerlenghi, A., Westbrooks, G. K., Consolaro, C., Cacho, I., Cesari, V., Cervera, C. S.: Record of methane emission from the West Svalbard continental margin during the last 23.5 ka revealed by $\delta^{13}C$ of benthic foraminifera, Global Planet. Change, 122, 151–160, 2014b.
Peltier, W. R. and Fairbanks, R. G.: Global glacial ice volume and Last Glacial Maximum duration from an extended Barbados sea level record, Quaternary Sci. Rev., 25, 3322–3337, 2006.
Pena, L. D., Calvo, E., Cacho, I., Eggins, S., and Palejero, C.: Identification and removal of Mn-Mg-rich contaminant phases in foraminiferal tests: implications for Mg/Ca past temperature reconstructions, Geochem. Geophy. Geosy., 6, Q09P02, doi:10.1029/2005GC000930, 2005.
Pena, L. D., Cacho, I., Calvo, E., Palejero, C., Eggins, S., and Sadekov, A.: Characterization of contaminant phases in foraminifera carbonates by electron microprobe mapping, Geochem. Geophy. Geosy., 9, Q07012, doi:10.1029/2008GC002018, 2008.

CPD
10, 4191–4227, 2014

Petersen, C. J., Bünz, S., Hustoft, S., Mienert, J., and Klaeschen, D.: High-resolution P-Cable 3D seismic imaging of gas chimney structures in gas hydrated sediments of an Arctic sediment drift, Mar. Petrol. Geol., 27, 1981–1994, 2010.

Plaza-Faverola, A., Bünz, S., and Mienert, J.: Repeated fluid expulsion through sub-seabed chimneys offshore Norway in response to glacial cycles, Earth Planet. Sc. Lett., 305, 297–308, 2011.

Rasmussen, S. O., Andersen, K. K., Svensson, A. M., Steffensen, J. P., Vinther, B. M., Clausen, H. B., Siggaard-Andersen, M.-L., Johnsen, S. J., Larsen, L. B., Dahl-Jensen, D., Bigler, M., Röthlisberger, R., Fischer, H., Goto-Azuma, K., Hansson, M. E., and Ruth, U.: A new Greenland ice core chronology for the last glacial termination, J. Geophys. Res., 111, D06102, doi:10.1029/2005JD006079, 2006.

Rasmussen, T. L., Thomsen, E., Ślubowska, M. A., Jessen, S., Solheim, A., and Koç, N.: Paleoceanographic evolution of the SW Svalbard margin (76° N) since 20,000 ^{14}C yr BP, Quaternary Res., 67, 100–114, 2007.

Rasmussen, T. L., Thomsen, E., and Nielsen, T.: Water mass exchange between the Nordic seas and the Arctic Ocean on millennial time scale during MIS 4-MIS 2, Geochem. Geophy. Geosy., 15, 530–544, doi:10.1002/2013GC005020, 2014.

Rathburn, A. E., Pérez, M. E., Martin, J. B., Day, S. A., Mahn, C., Gieskes, J., Ziebis, W., Williams, D., and Bahls, A.: Relationships between the distribution and stable isotopic composition of living benthic foraminifera and cold methane seep biogeochemistry in Monterey Bay: California, Geochem. Geophy. Geosy., 4, 1106, doi:10.1029/2003GC000595, 2003.

Reagan, M. T. and Moridis, G. J.: Oceanic gas hydrate instability and dissociation under climate change scenarios, Geophys. Res. Lett., 34, L22709, doi:10.1029/2007GL031671, 2007.

Reeburgh, W. S.: Anaerobic methane oxidation: rate depth distributions in Skan Bay sediments, Earth Planet. Sc. Lett., 47, 345–352, 1980.

Reeburgh, W. S.: Oceanic methane biogeochemistry, Chem. Rev., 107, 486–513, 2007.

Reimer, P. J., Bard, E., Bayliss, A., Beck, J. W., Blackwell, P. G., Ramsey, C. B., Caitlin, E. B., Cheng, H., Edwards, R. L., Friedrich, M., Grootes, P. M., Guilderson, T. P., Haflidason, H., Hajdas, I., Hatté, C., Heaton, T. J., Hoffmann, D. L., Hogg, A. G., Hugen, K. A., Kaiser, K. F., Kromer, B., Manning, S. W., Niu, M., Reimer, R. W., Richards, D. A., Scott, E. M., Staff, R. A., Turney, C. S. M., and van der Plicht, J.: Intcal13 and Marine13 radiocarbon age calibration curves 0–50,000 years cal bp, Radiocarbon, 55, 1869–1887, 2013.

CPD
10, 4191–4227, 2014

Sarnthein, M., Van Kreveld, S., Erlenkeuser, H., Grootes, P. M., Kucera, M., Pflaumann, U., and Schulz, M.: Centennial-to-millennial-scale periodicities of Holocene climate and sediment injections off the western Barents shelf, 75° N, Boreas, 32, 447–461, doi:10.1111/j.1502-3885.2003.tb01227.x, 2003.

Screen, J. A. and Simmonds, I.: The central role of diminishing sea ice in recent Arctic temperature amplification, Nature, 464, 1334–1337, 2010.

Shakhova, N., Semiletov, I., Salyuk, A., Yusupov, V., Kosmach, D., and Gustafsson, Ö.: Extensive methane venting to the atmosphere from sediments of the East Siberian Arctic Shelf, Science, 327, 1246–1250, 2010.

Sloan, E. D.: Gas hydrates: review of physical/chemical properties, Energ. Fuel., 12, 191–196, 1998.

Smith, A. J., Mienert, J., Bünz, S., and Greinert, J.: Thermogenic methane injection via bubble transport into the upper Arctic Ocean from the hydrate-charged Vestnesa Ridge, Svalbard, Geochem. Geophy. Geosy., 15, 1945–1959, doi:10.1002/2013GC005179, 2014.

Smith, L. M., Sachs, J. P., Jennings, A. E., Anderson, D. M., and deVernal, A.: Light δ^{13}C events during deglaciation of the East Greenland continental shelf attributed to methane release from gas hydrates, Geophys. Res. Lett., 28, 2217–2220, 2001.

Spielhagen, R. F., Wermer, K., Aagaard-Sørensen, S., Zamelczyk, K., Kandiano, E., Budeus, G., Husum, K., Marchitto, T. M., and Hald, M.: Enhanced modern heat transfer to the Arctic by warm Atlantic water, Science, 331, 450–453, 2011.

Stanford, J. D., Hemingway, R., Rohling, E. J., Challenor, P. G., Medina-Elizalde, M., and Lester, A. J.: Sea-level probability for the last deglaciation: a statistical analysis of far-field records, Global Planet. Change, 79, 193–203, 2011.

Stuiver, M., Reimer, P. J., and Reimer, R. W.: CALIB Radiocarbon Calibration, Execute Version 7.0html, available at: http://calib.qub.ac.uk/calib/ (last access: 18 August 2014), 2014.

Sztybor, K., Rasmussen, T. L., Mienert, J., Bünz, S., and Consolaro, C.: Methane release from the seabed and reliability of the paleorecord, 12th International Conference on Gas in Marine Sediments (GIMS12th), Taipei, Taiwan, 1–6 September 2014, (oral presentation), 2014.

Torres, M. E., Mix, A. C., Kinports, K., Haley, B., Klinkhammer, G. P., McManus, J., and de Angelis, M. A.: Is methane venting at the seafloor recorded by δ^{13}C of benthic foraminifera shells?, Paleoceanography, 18, 1062, doi:10.1029/2002PA000824, 2003.

Torres, M. E., Martin, R. A., Klinkhammer, G. P., and Nesbitt, E.: Post depositional alteration of foraminiferal shells in cold seep settings: new insights from flow-through time-resolved

CPD
10, 4191–4227, 2014

analysis of biogenic and inorganic seep carbonates, Earth Planet. Sc. Lett., 299, 10–22, 2010.
Vogt, P. R., Crane, K., Sundvor, E., Max, M. D., and Pfirman, S. L.: Methane-generated (?) pockmarks on young, thickly sedimented oceanic crust in the Arctic: Vestnesa ridge, Fram strait, Geology, 22, 255–258, 1994.
Volkmann, R. and Mensch, M.: Stable isotope composition (δ^{18}O, δ^{13}C) of living planktic foraminifers in the outer Laptev Sea and the Fram Strait, Mar. Micropaleontol., 42, 163–188, 2001.
Wallmann, P., Mahood, G., and Pollard, D.: Mechanical models for correlation of ring-fracture eruptions at Pantelleria, Strait of Sicily, with glacial sea-level drawdown, B. Volcanol., 50, 327–339, 1988.
Wefer, G., Heinze, P.-M., and Berger, W. H.: Clues to ancient methane release, Nature, 369, 282 doi:10.1038/369282a0, 1994.
Wollenburg, J. E., Kuhnt, W., and Mackensen, A.: Changes in Arctic Ocean paleoproductivity and hydrography during the last 145 kyr: the benthic foraminiferal record, Paleoceanography, 16, 65–77, 2001.

CPD
10, 4191–4227, 2014

Table 1. Radiocarbon data and sedimentation rate[a].

Depth (cm bsf)	Dated material	Laboratory reference	AMS ^{14}C dates (years BP)	Calibrated age (cal years BP, $\pm 2\sigma$ median)	δ^{13}C (‰)	Sed. rate (cm ka^{-1})
5–7	*N. pachyderma* (s)	UBA-19 355	848 ± 29	470 ± 50	−1.2	18.75
60–61	*N. pachyderma* (s)	UBA-18 143	3477 ± 36	3340 ± 100	−1.6	18.82
170–171	*N. pachyderma* (s)	UBA-19 356	7001 ± 33	7490 ± 70	−1.1	26.51
250–251	*N. pachyderma* (s)	UBA-18 144	8707 ± 39	9370 ± 100	−0.6	42.55
335–337	*N. pachyderma* (s)	UBA-19 357	10 130 ± 47	11 110 ± 130	−0.7	49.43
360–361	*N. pachyderma* (s)	UBA-18 145	11 203 ± 45	12 690 ± 110	−1.3	17.85
363–367	*N. pachyderma* (s)	UBA-19 358	11 250 ± 57	12 735 ± 130	−1.5	17.85
413–418	*N. pachyderma* (s)	UBA-18 146	12 575 ± 51	14 040 ± 150	−1.1	38.32

[a] Radiocarbon data and calibrated ages in core JM10-330GC together with the calculated linear sedimentation rate.

CPD
10, 4191–4227, 2014

Table 2. Energy Dispersive X-ray Spectroscopy (EDS) data*.

EDS number	Species	Depth (cm bsf)	Age (cal years BP)	$\delta^{13}C$ (‰VPDB)	$\delta^{18}O$ (‰VPDB)	Ca (wt%)	Mg (wt%)	Na (wt%)	K (wt%)	Al (wt%)	Fe (wt%)	Si (wt%)
1 (Fig. 6b)	Nps	390	13 375	−2.61	5.26	96.75	0.7	0.7	–	0.45	–	1.4
2 (Fig. 6c)	Nps	390	13 375	−2.61	5.26	6.4	8.1	2.4	9.7	16.7	15.7	41
3 (Fig. 6c)	Nps	390	13 375	−2.61	5.26	8.55	7.5	2.25	8.9	17.1	16.3	39.4
4 (Fig. 6c)	Nps	390	13 375	−2.61	5.26	99.17	–	0.83	–	–	–	–
5 (Fig. 6c)	Nps	390	13 375	−2.61	5.26	99.36	–	0.64	–	–	–	–
6 (Fig. 6e)	Nps	295	10 270	−0.02	3.21	97	0.55	1.9	–	–	–	0.55
7 (Fig. 6f)	Nps	295	10 270	−0.02	3.21	99.72	–	0.28	–	–	–	–
8 (Fig. 6f)	Nps	295	10 270	−0.02	3.21	98	–	1	–	–	–	1
9 (Fig. 6f)	Nps	295	10 270	−0.02	3.21	98.2	0.4	0.6	–	0.4	–	0.4
10 (Fig. 6h)	Nps	80	4103	0.68	3.47	99.8	–	0.2	–	–	–	–
11 (Fig. 6i)	Nps	80	4103	0.68	3.47	99.5	–	0.5	–	–	–	–
12 (Fig. 6i)	Nps	80	4103	0.68	3.47	99.6	–	0.4	–	–	–	–
13 (Fig. 7k)	Cneot	390	13 375	−4.37	5.26	98.4	–	1.6	–	–	–	–
14 (Fig. 7l)	Cneot	390	13 375	−4.37	5.26	97.25	0.5	1.75	–	0.5	–	–
15 (Fig. 7l)	Cneot	390	13 375	−4.37	5.26	98.5	–	1	–	0.5	–	–
16 (Fig. 7n)	Cneot	295	10 270	−3.41	5.15	99.5	–	0.5	–	–	–	–
17 (Fig. 7n)	Cneot	295	10 270	−3.41	5.15	99.5	–	–	–	–	–	0.5
18 (Fig. 7n)	Cneot	295	10 270	−3.41	5.15	96	0.73	0.74	–	0.73	–	1.8
19 (Fig. 7o)	Cneot	295	10 270	−3.41	5.15	98.7	–	1	–	–	–	0.3
20 (Fig. 7q)	Cneot	80	4103	−0.44	4.49	99.3	–	0.7	–	–	–	–
21 (Fig. 7r)	Cneot	80	4103	−0.44	4.49	99.5	–	0.5	–	–	–	–
22 (Fig. 7r)	Cneot	80	4103	−0.44	4.49	99.4	–	0.6	–	–	–	–

* EDS qualitative estimates of major trace metal contents of foraminifera carbonate test in both depleted (390 and 295 cm bsf) and non-depleted (80 cm bsf) ^{13}C intervals.
Nps: *N. pachyderma* (s); Cneot: *C. neoteretis.*

CPD
10, 4191–4227, 2014

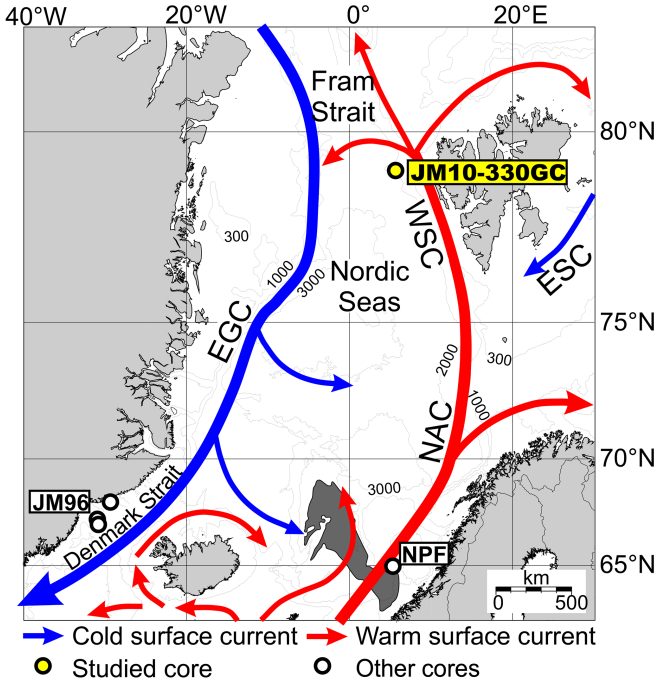

Figure 1. Bathymetric map of the Nordic seas showing the major surface currents and the location of studied core JM10-330GC (yellow circle), the location of cores described by Smith et al. (2001) (JM96, white circles), and of the cores described by Hill et al. (2012) in the Nyegga pockmark field (NPF, white circle) next to the Storegga Slide (dark grey area) on the mid-Norwegian margin. Abbreviations: NAC: North Atlantic Current; WSC: West Spitsbergen Current; ESC: East Spitsbergen Current; EGC: East Greenland Current.

CPD
10, 4191–4227, 2014

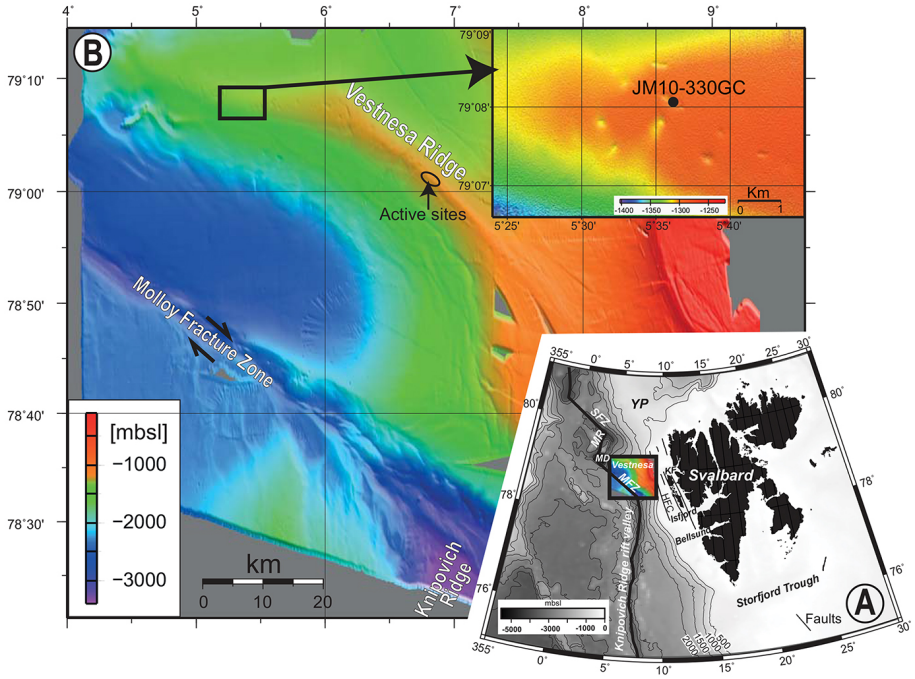

Figure 2. (a) Bathymetric map of the W-Svalbard margin and eastern Fram Strait. Abbreviations: MFZ: Molloy Fracture Zone; MD: Molloy Deep; MR: Molloy Ridge; SFZ: Spitsbergen Fracture Zone; YP: Yermak Plateau. **(b)** Overview swath bathymetry map of the Vestnesa Ridge. Locations of studied core JM10-330GC and location of active sites with gas flares observed in June 2010 (Bünz et al., 2012) and in 2012 (Smith et al., 2014) are indicated. Figures are modified after Hustoft et al. (2009a).

CPD
10, 4191–4227, 2014

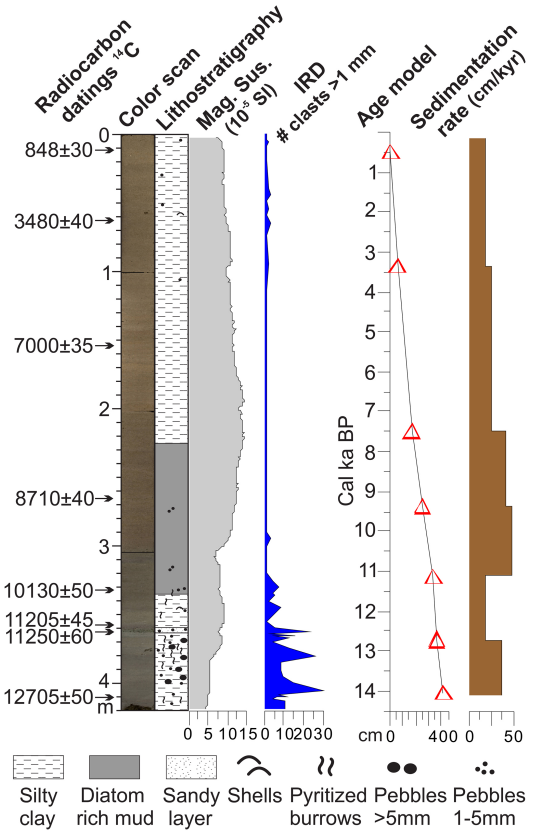

Figure 3. On the left: lithology and color scan of core JM10-330GC, together with magnetic susceptibility and concentration of ice-rafted debris (IRD) per gram dry weight sediment. Arrows indicate positions of original radiocarbon dates. On the right: age model and calculated sediment accumulation rates. Red triangles indicate radiocarbon dates.

CPD
10, 4191–4227, 2014

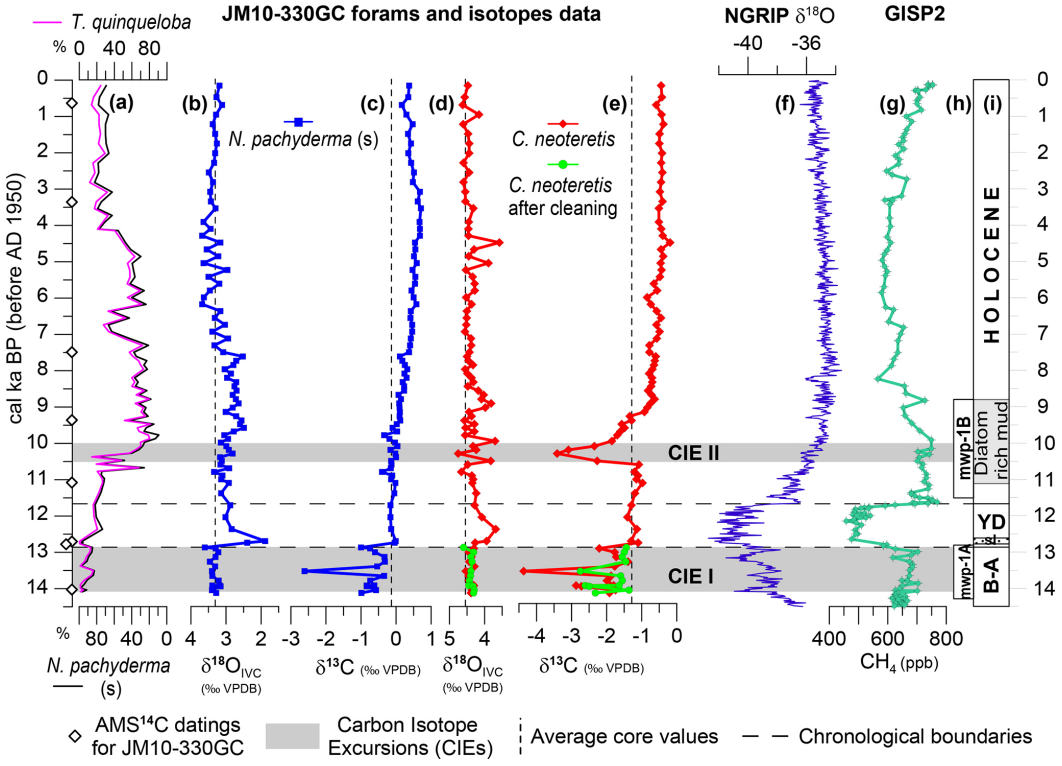

CPD
10, 4191–4227, 2014

Carbon isotope excursions in Fram Strait during the last 14 ka

C. Consolaro et al.

Figure 4. (a–e) Planktic foraminifera and geochemical data of core JM10-330GC plotted vs. calibrated (cal) ka before present (BP); **(a)** relative abundance of *Neogloboquadrina pachyderma* (s) (black line) and *Turborotalita quinqueloba* (purple line); **(b)** ice volume corrected (IVC) $\delta^{18}O_{IVC}$ record of *N. pachyderma* (s); **(c)** $\delta^{13}C$ record of *N. pachyderma* (s); **(d)** $\delta^{18}O_{IVC}$ record of *Cassidulina neoteretis* before (red line) and after (green line) the cleaning protocol of Pena et al. (2005); **(e)** $\delta^{13}C$ record of *C. neoteretis* before (red line) and after (green line) the cleaning protocol of Pena et al. (2005). Dotted vertical lines indicate average core values. **(f–h)** Other records: **(f)** NorthGRIP ice core $\delta^{18}O$ record (North Greenland Ice Core Project Members, 2004); **(g)** Greenland Ice Sheet Project 2 (GISP2) atmospheric CH_4 record (Brook et al., 2000); **(h)** melt water pulse mwp-1A and mwp-1B (Peltier and Fairbanks, 2006; Stanford et al., 2011); **(i)** stratigraphy obtained for JM10-330GC with chronological subdivisions. White diamonds on the *y* axis indicate AMS ^{14}C dating points for JM10-330GC. Shaded horizontal bars indicate carbon isotope events CIE I and CIE II. Dashed lines represents chronological boundaries. Abbreviations: B–A: Bølling–Allerød; YD: Younger Dryas; sl: sandy layer.

CPD
10, 4191–4227, 2014

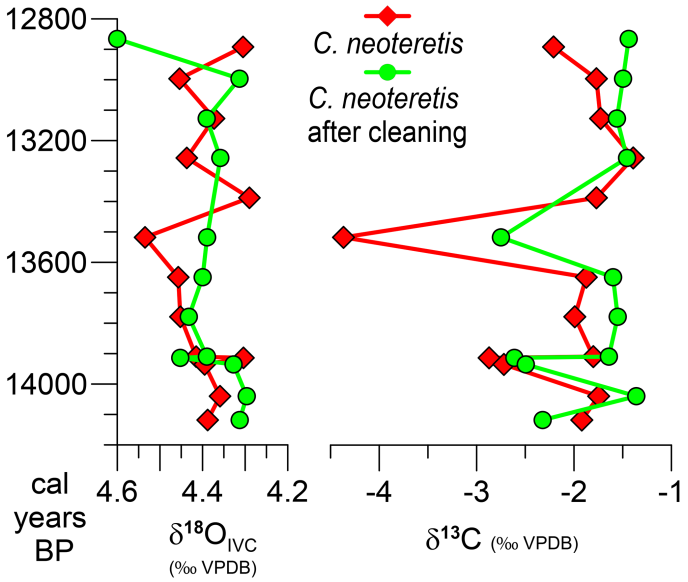

Figure 5. Detail of the δ^{18}O and δ^{13}C record of *C. neoteretis* before (red line) and after (green line) the cleaning protocol of Pena et al. (2005).

CPD
10, 4191–4227, 2014

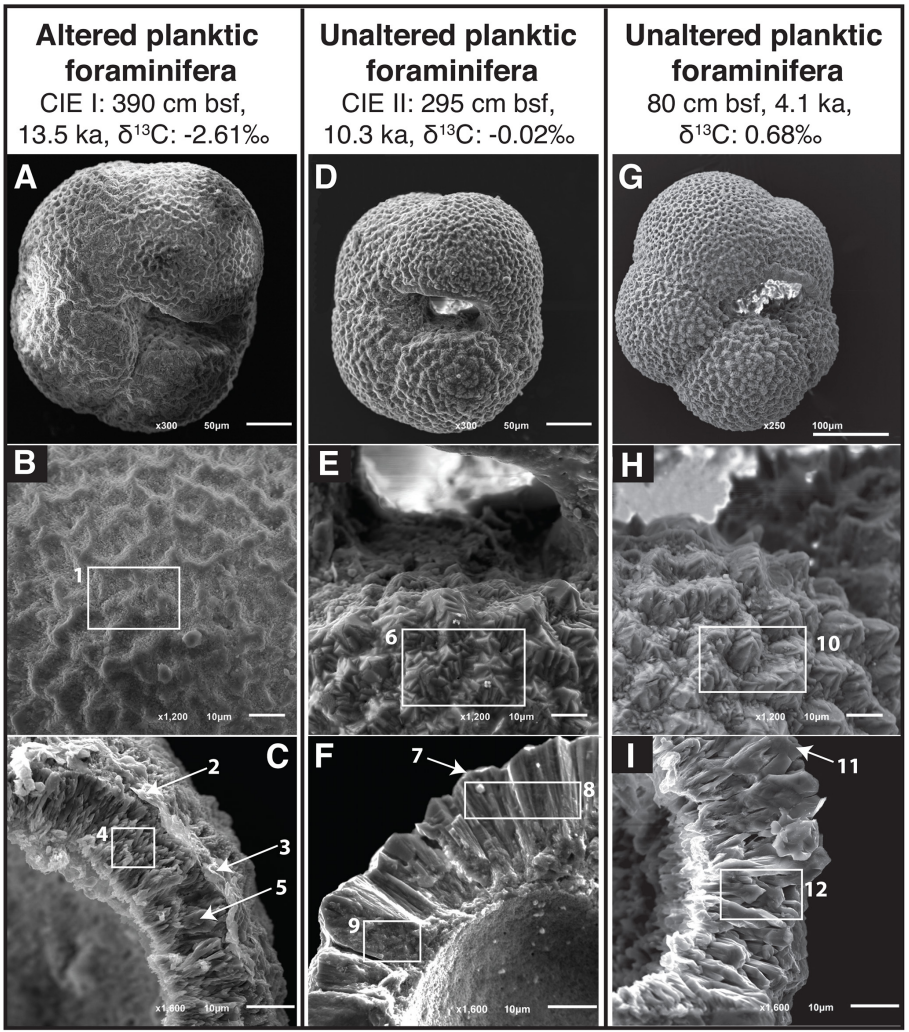

CPD
10, 4191–4227, 2014

Carbon isotope excursions in Fram Strait during the last 14 ka

C. Consolaro et al.

Figure 6. SEM images on selected representative specimens of *N. pachyderma* (s) from different intervals: **(a)**, **(b)** and **(c)** from 390 cm bsf; **(d)**, **(e)** and **(f)**, from 295 cm bsf; **(g)**, **(h)**, and **(i)** from 80 cm bsf. The numbers in the pictures indicate EDS analyses in Table 2. **(a)** *N. pachyderma* (s) test from the most depleted interval within CIE I (δ^{13}C: −2.61 ‰, 13.5 ka, 390 cm bsf), showing an altered test. **(b)** Detail of **(a** with clearly altered external surface. **(c)** Broken test of a different specimen of *N. pachyderma* (s) from the same interval where the foraminiferal wall shows a pristine structure but with a thin deposited layer (methane-derived coating) unevenly covering the external text. **(d)** *N. pachyderma* (s) from CIE II interval (δ^{13}C: −0.02 ‰, 10.3 ka, 295 cm bsf) showing an unaltered test. **(e)** Detail of **(d)** with pristine shell structure. **(f)** Detail of the wall structure with pristine crystal palisades from a different specimen in the same interval. **(g)** *N. pachyderma* (s) from interval with normal ^{13}C values (δ^{13}C: 0.68 ‰, 4.1 ka, 80 cm bsf) showing a well-preserved test with pristine shell structure. **(h)** Detail of **(g)** with pristine crystals shape. **(i)** Detail of the wall structure with pristine crystal palisades from a different specimen in the same interval. Picture magnifications and length of the white bar are indicated in each picture.

CPD
10, 4191–4227, 2014

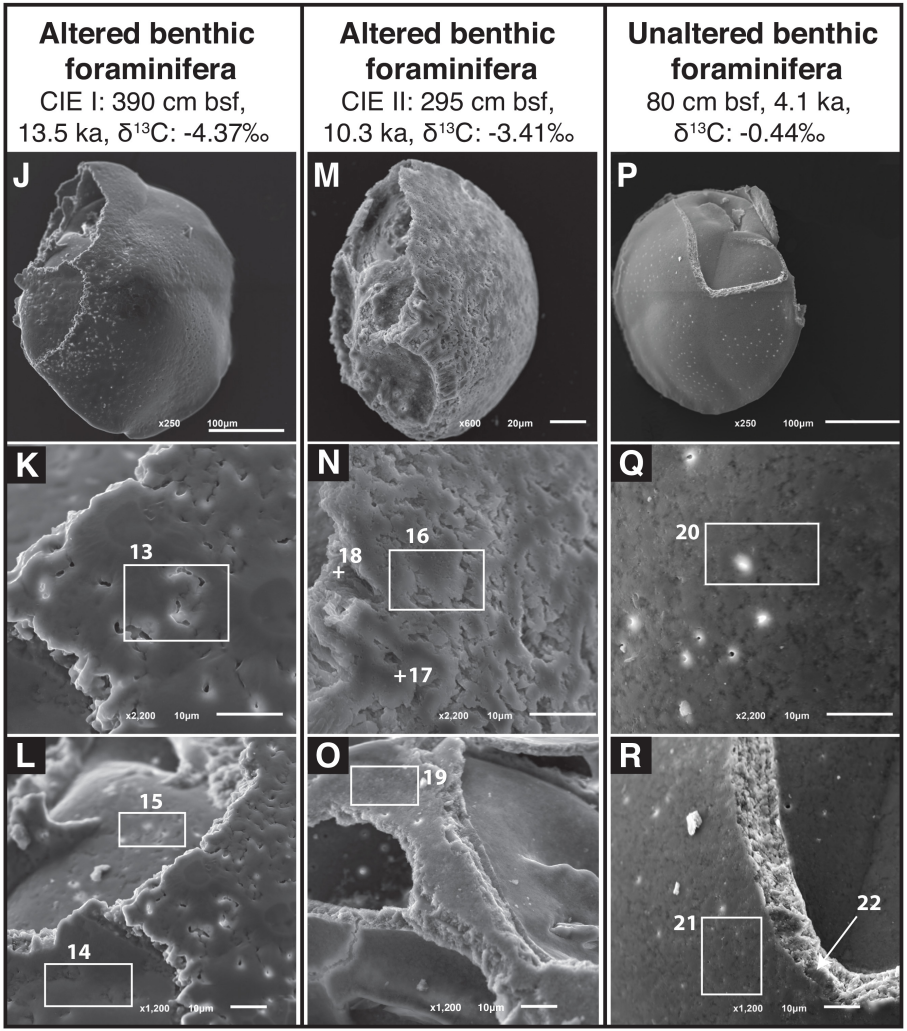

CPD
10, 4191–4227, 2014

Carbon isotope excursions in Fram Strait during the last 14 ka

C. Consolaro et al.

Figure 7. SEM images on selected representative specimens of *C. neoteretis* from the altered intervals (**j**, **k** and **l** from 390 cm bsf; **m**, **n** and **o**, from 295 cm bsf) and from an interval with normal ^{13}C values (**p**, **q**, and **r** from 80 cm bsf). The numbers in the pictures indicate EDS analyses in Table 2. **(j)** *C. neoteretis* test from the most depleted interval within CIE I ($\delta^{13}C$: −4.37 ‰, 13.5 ka, 390 cm bsf), showing an altered test with dissolution and corrosion features. **(k)** Detail of **(j)** where the external test shows enlarged pores (5–7 µm) with irregular shapes giving to the test a cauliflower appearance. **(l)** Detail of **(j)** with a different magnification showing the cauliflower appearance and the irregular profile of the test wall. **(m)** *C. neoteretis* from CIE II interval ($\delta^{13}C$: −3.41 ‰, 10.3 ka, 295 cm bsf) showing an altered test with dissolution and corrosion features. **(n)** Detail of **(m)** where the cauliflower appearance due to enlarged and irregular shaped pores is evident and widespread. **(o)** Detail of the test of a different specimen from the same interval, where the alteration is less evident with no cauliflower appearance but the profile of the test walls is quite irregular. **(p)** *C. neoteretis* from an interval with normal ^{13}C values ($\delta^{13}C$: −0.44 ‰, 4.1 ka, 80 cm bsf) showing a well-preserved test with pristine shell structure. **(q)** Detail of **(p)** showing small (< 1µm) and round shape pores with no alteration features. **(r)** Detail of **(p)** with a different magnification showing a well preserved test and regular profile of the test wall. Picture magnifications and length of the white bar are indicated in each picture.

CPD
10, 4191–4227, 2014